JOURNAL OF GEOPHYSICAL RESEARCH, VOL. 91, NO. B11, PAGES 11,407-11,419, OCTOBER 10, 1986

THE EFFECTS OF CHEMICAL DENSITY DIFFERENCES ON CONVECTIVE MIXING IN THE EARTH'S MANTLE

Michael Gurnis

Research School of Earth Sciences, Australian National University, Canberra

Abstract. Subducted lithosphere and crust are chemically distinct from ambient mantle, and some have hypothesized that the resulting anomalous buoyancy may affect mixing and, in particular, may cause chemical heterogeneity to persist. To explore this effect, two-dimensional convective mixing calculations have been carried out. Boundary conditions mimicking features of plate kinematics have been imposed and negatively buoyant tracers placed beneath converging plate margins to simulate subduction. The principal parameter of interest is the density anomaly ratio: $\Delta\rho/(\rho_0 \alpha \Delta T)$, the ratio of the chemical to the thermal buoyancy. For a density anomaly ratio appropriate to complete separation of the oceanic crust from the rest of the lithosphere, it is marginally possible for the tracers to segregate into the warm region near the bottom and neutralize the thermal buoyancy there, for internally heated flows, and to segregate to the base of the uprising limbs of convection, for bottom heated flows. However, for the more likely scenario of oceanic crust and lithosphere maintaining their layering after subduction, there is neither segregation nor neutralization of thermal buoyancy. The average residence time is the average time tracers remain in the box from subduction to sampling beneath ridges and could be increased by 4% from the passive case at the very most if the crust and lithosphere remain layered. Even in the more extreme case of separation of crust from lithosphere, the residence times are only increased by 15% from the passive case.

Introduction

The isotopic heterogeneity of mantle-derived oceanic basalts has pointed to the existence of several or even many chemical reservoirs within the mantle which have remained distinct for billions of years [Hofmann and White, 1982; Brooks et al., 1976]. Although this is expressed qualitatively, it is a robust constraint on mantle models but, unfortunately, difficult to reconcile with the observation of a convecting mantle (i.e., convection manifest by lithospheric motions). Some investigators have hypothesized that because subducting lithosphere is chemically different from ambient mantle, and hence may have different intrinsic density, it preferentially segregates to particular zones or layers within the mantle and that this process maintains chemical heterogeneity within the mantle for billions of years [Anderson, 1982; Hofmann and White, 1982; Ringwood, 1982]. For example, Hofmann and White [1982] hypothesize that because subducting oceanic crust transforms to eclogite, which is intrinsically more dense than ambient mantle, it separates from the lower lithosphere, sinks to the core-mantle boundary (CMB) and forms a layer on a time scale of hundreds of millions to billions of years. The purpose of this paper is to evaluate the general physical processes envisaged in such hypotheses [Anderson, 1982; Hofmann and White, 1982; Ringwood, 1982] with simplified computations; it is hoped that the calculations will shed light onto the viability of some models and eliminate those models incapable of segregating in the ways assumed. In addition, the calculations should further our understanding of the dynamics of fluids with mantle properties.

The hypotheses advanced by Anderson [1982], Hofmann and White [1982], and Ringwood [1982] fail to consider the likely effects of large-scale mantle flow. This should not so much be seen as criticism of these modeling efforts but rather indicating a gap in our understanding of how chemical and thermal buoyancy interact. The problem addressed can be expressed simply as, Are the buoyancy forces caused by intrinsic density large enough to offset locally the thermal buoyancy forces that drive the large-scale flow and therefore have an appreciable effect on mantle dynamics and evolution?

Mixing phenomena will be studied by using two-dimensional convection calculations, which are primarily driven by thermal buoyancy but perturbed by chemical buoyancy. The flow is constrained by known features of mantle convection, most importantly the features of plate kinematics: the uniform horizontal velocity across plates, the symmetrical spreading at ridges, and the asymmetrical convergence at trenches. In addition, the effect of the time dependence of plate kinematics (i.e., ridge and trench migration and plate rearrangements) is fully explored. Tracers are introduced below the "trenches" and sampled beneath the "ridges" to simulate mantle recycling. The case where the tracers are passive (neutrally buoyant) has been investigated by Gurnis and Davies [1986], hereafter, paper 1; the purpose of this paper is to study the case of negatively buoyant (heavy) tracers.

This paper is organized so that the discussion of mathematical concepts and numerical procedures is left for the appendices. Before the fully numerical results are given, (simple) Stokes velocity calculations are presented to clarify the regimes in which intrinsic density could play a role in mantle dynamics. In the subsequent section the parameter values for the computations are then outlined and justified. The setup of the models is then summarized, and this is followed by a systematic presentation of the numerical results. The effect intrinsic buoyancy has on the residence times of subducted material follows. Finally, the nondimensional results are scaled to the mantle.

Paper number 5B5885.
0148-0227/86/005B-5885$05.00

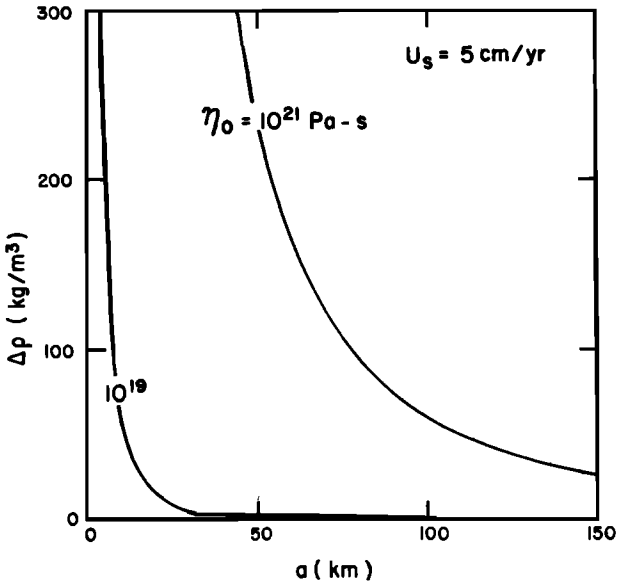

Fig. 1. Radii a and density differences $\Delta\rho$ necessary for a fluid sphere to achieve a velocity of 5 cm/yr. The average viscosity for the whole mantle is approximately 10^{21} Pa s; $\eta_0 = 10^{19}$ Pa s should be considered implausibly small. These calculations demonstrate that small-scale (~ 10 km) anomalies cannot achieve velocities comparable to velocities of mantle convection.

Simple Stokes Velocity Calculations

The purpose of this section is to outline, with simple calculations, the sizes and intrinsic densities needed to achieve velocities comparable with lithospheric velocities. In this section, a spherical heterogeneity of radius a, density ρ_s, and dynamic viscosity η_s, is considered. The terminal velocity, with Reynolds number much less than unity, is [Batchelor 1967]

$$U_s = \frac{1}{3} \frac{a^2 g f_m}{\nu_0} \frac{\rho_s - \rho_0}{\rho_0} \Upsilon(\eta) \qquad (1)$$

$$\Upsilon(\eta) = \frac{\eta_0 + \eta_s}{\eta_0 + \frac{3}{2}\eta_s} \qquad (2)$$

where ρ_0 and η_0 are the density and dynamic viscosity of the ambient mantle ($\nu_0 = \eta_0/\rho_0$ is the kinematic viscosity); f_m is the mixing fraction and denotes the fraction of chemically anomalous material (with ρ_s) mixed through the volume of radius a. For the case of a heterogeneity within the mantle, we would expect $\eta_0 \approx \eta_s$ and thus $\Upsilon(\eta) = 4/5$.

The first point that will be demonstrated is that the velocities of small (~ 10 km) sized heterogeneities are much smaller than average plate velocities (~ 5 cm/yr) unless unrealistically large intrinsic densities are assumed. The high-pressure mineral assemblage with the largest $\Delta\rho$ (through the upper mantle) is eclogite and, at most, has a value of 200 kg m^{-3} [Anderson, 1979; Ringwood, 1975, 1982]. It seems unlikely that $\Delta\rho$ could be much larger than this anywhere in the mantle. As will become clear, the ambient mantle viscosity is a principal quantity affecting the velocities. There seemed to have been consensus that the effective (Newtonian) viscosity was approximately uniform throughout the mantle and with a value of about 10^{21} Pa s [Cathles, 1975; Peltier, 1981]. However, within the last few years, new evidence suggests that the viscosity may be even larger in the lower mantle (perhaps by a factor of 10 or more) [Hager, 1984; O'Connell and Hager, 1984; Yuen et al., 1982].

In Figure 1, the $\Delta\rho$ required for a sphere of radius a to achieve a velocity of 5 cm/yr is plotted. For example, a sphere of radius 75 km would need an excess density of at least 100 kg m^{-3} throughout, for it to achieve a velocity of 5 cm/yr. This clearly demonstrates that small heterogeneities cannot move at plate velocities through a fluid of $\eta_0 = 10^{21}$ Pa s without assuming unrealistically large intrinsic densities. Small heterogeneities could move at plate velocities if η_0 was low enough, as is shown by the curve for $\eta_0 = 10^{19}$ Pa s (the value assumed by Anderson [1982]), but from the references cited, this viscosity must be considered as unrealistically low.

In Figure 2, Stokes velocities are plotted as a function of radius a, and mixing fraction f_m, when $\Delta\rho$ = 200 kg m^{-3}. This plot clearly shows that large-scale regions with reasonable volumes of ambient mantle and with "anomalously" dense material mixed through, could reach velocities approaching lithospheric plates. For example, a volume of 500-km radius and with 1% eclogite coarsely mixed through it can move at 4 cm/yr. This volume of eclogite is produced in less than 1/2 m.y. (million years), globally, assuming an areal rate of plate subduction of 3 km^2/yr [Chase, 1972] and an oceanic crustal depth of 6 km.

In certain parts of the flow, convective

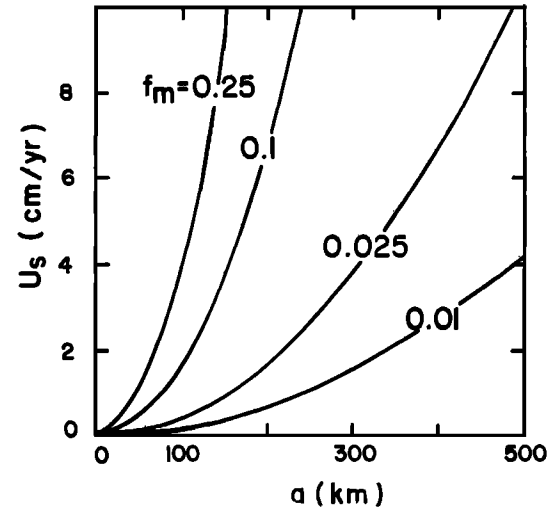

Fig. 2. Stokes velocities U_s as a function of sphere radius a. Each curve is for a density difference of $f_m\Delta\rho$, where $\Delta\rho$ = 200 kg m^{-3}. The viscosity is 10^{21} Pa s in all cases; f_m is the mixing fraction. These calculations demonstrate that very large anomalies (> 200 km across) can achieve significant velocities if material with an excess density of 200 kg m^{-3} is mixed with $f_m > 0.01$ through the region.

TABLE 1. Primary Quantities

Quantity	Description	Value	Reference
g	Gravitational acceleration	10 m s^{-2}	
α	Coefficient of thermal expansion	2×10^{-5} K^{-1}	Turcotte and Schubert [1982]
K	Thermal conductivity	3 W K^{-1} m^{-1}	Turcotte and Schubert [1982]
κ	Thermal diffusivity	10^{-6} m^2 s^{-1}	Turcotte and Schubert [1982]
ρ_o	Ambient density		
	Whole mantle	4000 kg m^{-3}	Turcotte and Schubert [1982]
	Upper mantle	3500 kg m^{-3}	Turcotte and Schubert [1982]
D	Depth of convection		
	Whole mantle	3×10^6 m	
	Upper mantle	7×10^5 m	
η	Average viscosity	10^{21} Pa s	Peltier [1981]
q	Surface heat flux	0.080 W m^{-2}	Davies [1980]
ΔT	Temperature across lithosphere	1400 K	Cazenave [1984] and Parsons and Sclater [1977]
U	Average horizontal velocity	5 cm yr^{-1}	Chase [1972]

velocities may be less than the average velocity used for these calculations, and more segregation could take place than is indicated here. For example, near the lower boundary, vertical convective velocities could be smaller than the Stokes velocities of small chemical blobs.

These simple calculations suggest how the more intensive numerical models should be set up, on the one hand, and the type of phenomena that could be expected, on the other. Intrinsic density (with realistic ρ_s) can only give rise to appreciable velocities if the anomaly exists over a fairly large length scale (hundreds of kilometers). In terms of the numerical calculations, this means we can use a fairly coarse grid without loss of resolution of important mixing phenomena. We need only look for mixing phenomena that tend to concentrate the tracers over a fairly large volume.

Controlling Parameters and Assigned Values

The mixing phenomena displayed in the models presented here are affected by the buoyancy generated by chemical density differences, on the one hand, and the thermal buoyancy, on the other. The effect of the chemical buoyancy is controlled by the density difference of the anomalous material, the volume flux of this material into the convecting system, and the time over which the anomalous material has entered the system (i.e., approximately the total mass of the anomalous material). To a lesser extent, the mixing is affected by the mode of heating and the imposed boundary velocity. Expressions describing these fluid parameters and the values assigned to them are given below.

Chemical Rayleigh number. The chemical buoyancy is measured by a "chemical Rayleigh" number Rc defined as

$$Rc = \frac{g \Delta\rho D^3}{\rho_o \kappa \nu} \tag{3}$$

where D is the depth of the convecting system, $\Delta\rho$ is the density difference between ambient or average mantle ρ_o and a chemical heterogeneity, and κ is the thermal diffusivity.

Thermal Rayleigh number. The thermal Rayleigh number is defined as

$$Ra = \frac{g \alpha \Delta T D^3}{\kappa \nu} \tag{4}$$

where α is the volumetric coefficient of thermal expansion and ΔT is a temperature scale associated with the large-scale flow. For the numerical computations, Ra is defined in terms of the total heat flux, and a temperature scale $\Delta T = QD/K$ is defined. Ra is thus redefined as

$$R_Q = \frac{g \alpha D^4 Q}{K \kappa \nu} \tag{5}$$

where Q is the total heat transported. Using the parameter values in Table 1, R_Q is approximately 2.6×10^9 and 6.7×10^6 for whole-mantle and upper mantle convection, respectively. With such high R_Q, the thermal boundary layers are thin and give rise to time-dependent instabilities [McKenzie et al., 1974]. Following the procedure in paper 1 and in Davies [1986], R_Q has been scaled downward to inhibit small-scale instabilities, on the one hand, and to allow accurate calculation of the flow with a small number of mesh points, on the other. All the computations were carried out at $R_Q = 10^5$.

Heating mode. The ratio of internal to total heating is μ (defined in Appendix A) and takes

on either a value of zero for entirely bottom heating or a value of 1 for entirely internal heating.

Boundary velocity. The boundary velocity is imposed on the top surface of the box, as described in the subsequent section, and is controlled by the Peclet number Pe, defined in Appendix A. For most of the calculations presented here, Pe=100 with some at 50; the choice of a particular Pe value is described at length in paper 1. In general, however, the Pe chosen is near the free convective velocity arising from the thermal buoyancy, and the principal effect of this parameter is to organize the flow.

Density anomaly ratio. The ratio of the chemical to thermal buoyancy is the density anomaly ratio:

$$A = \frac{Rc}{Ra} = \frac{\Delta\rho}{\rho_o \alpha \Delta T} \tag{6}$$

If ΔT is an actual temperature difference, between either the top and bottom of the box (e.g., $T_b - T_t$) or across a boundary layer, then we have

$$A_T = \frac{\Delta\rho}{\rho_o \alpha (T_b - T_t)} \tag{7}$$

With this definition, the value of A_T at the transition between different mixing regimes (i.e., when layering first sets in, for example) should be independent of the Rayleigh number.

A transition value of A_T is independent of R_Q if the mode of convection remains independent of R_Q. In general, as R_Q increases, the aspect ratio of convection cells generally decreases, and the flow unsteadiness increases because of the growth of boundary layer instabilities [McKenzie et al., 1974]. Because of the temperature sensitivity of mantle viscosity, however, the instabilities of the top thermal boundary layer are strongly inhibited from growing [Yuen et al., 1981], and thus small-scale instability is much less dependent on R_Q than it would be in a constant viscosity medium. A transition value of A_T is thus assumed independent of R_Q as a simple place to begin this investigation.

For the numerical computations, ΔT in (6) is again expressed in terms of the total heat flux, as was done for the Rayleigh number. The appropriate density anomaly ratio then is

$$A_Q = \frac{\Delta\rho\ K}{\rho_o \alpha Q D} \tag{8}$$

With this definition, transition values of the density anomaly ratio will depend on the Rayleigh number, R_Q (see Appendix C). Values of A_Q quoted in the results section apply to the model. In the final section, these parameters will be scaled to the mantle, which has a higher R_Q; it is best for the moment to defer the discussion of scaling to the mantle until after the basic fluid dynamics have been considered. A_Q is taken as a free (or independent) variable. Initially, A_Q is zero but then is increased to carefully document the mixing phenomena, in particular, to document the values of A_Q when certain phenomena set in.

Volume flux. The mixing is also affected by the rate at which anomalous material is injected into the convecting system and also the total time duration of that injection. The areal rate of the injection is defined as

$$\dot{s} = \delta w\ u_b = \delta w \frac{Pe}{Ra} \tag{9}$$

where δw is the nondimensional depth of the anomalous material and u_b is the characteristic boundary velocity (see Appendix A); δw has been held constant at 0.002 for all computed cases, and this corresponds to the injection of a 6-km layer of anomalous material in a system 3000 km deep. Since most cases were carried out at $R_Q = 10^5$ and Pe = 100, $\dot{s} = 2 \times 10^{-6}$. Here $\dot{s}$ was the same in all but two cases; this was done because there is a simple trade-off between the flux $\dot{s}$ and A_T (see Appendix B), which allows the model results to be simply scaled to other values of δw.

Moreover, the length of time anomalous material is introduced into the convecting system is also varied. In most cases, the anomalous material is introduced over the first 10 transit times (see below) of the model run, but in some additional cases the material was introduced through the entire model run.

Model times. The model times are discussed in terms of transit times; one transit time is defined as the time to traverse the box depth with the average imposed plate velocity. With mantle parameters, one transit time is equivalent to approximately 14 m.y. for upper mantle and 60 m.y. for whole mantle convection. The models were run for 10 to more than 100 transit times.

Setup of Numerical Computations

These calculations bear many similarities to those presented in paper 1, and more detailed information can be found in that paper; with the use of intrinsic density, the equations of motion and numerical procedure are modified somewhat from the earlier work, and these changes are outlined in Appendix A. Moreover, the code was checked out by calculating the fall of an infinitely long cylinder and comparing it with the calculations and experiments presented by Richter [1977].

The equations of motion are solved in a two-dimensional rectangle, and velocity boundary conditions are imposed on the top to reproduce various features of plate kinematics. The resulting flows are intended to represent the large-scale mantle flow associated with plate motion. Beneath a converging plate margin, negatively buoyant tracers are introduced to simulate the subduction of chemically anomalous material. The tracers are sampled near the ridge to simulate the re-incorporation of the mantle into the lithosphere (recycling). This is discussed quantitatively in Appendix B. Most of the cases were carried out with (n times m) 15 x 63 meshes, while in some cases 31 x 127 meshes were used to test the reproducibility of the results.

It must be emphasized what these calculations can and cannot tell us. They are not simulations of the mantle. Because of the coarseness of the mesh used, detailed mechanics of the subducted

TABLE 2. Summary of Mixing Computations With Intrinsic Density

Case	Plate Model	n	μ	Pe	A_Q	$N_{\bar{T}}$	$A_{\bar{T}}$	N_m	Γ_{peak}	$\frac{\tau}{t_f}$	Run Time
1	s	15	1	100	0	10.7	0				30
2	s	15	1	100	2	10.5	21.0	100	0.51		30
3	s	15	0	100	2	6.0	24.0	100	0.73		40
4	a	15	1	100	0	8.2	0			1.08	400
5	a	15	1	100	1	8.2	8.2	100	0.35		90
6	a	15	1	100	2	8.1	16.2	100	0.34	1.80	100
7	a	31	1	100	2	8.4	16.8	25	0.76		20*
8	a	15	1	100	3	8.1	24.3	100	0.25	2.55	90
9	a	15	1	50	0	6.8	0			1.00	300
10	a	15	1	50	2	7.0	14.0	100	0.20	1.51	70
11	a	15	0	100	0	4.7	0			1.15	60
12	a	15	0	100	1	4.7	9.4	100	0.29	1.59	60
13	a	15	0	100	2	4.6	18.4	100	0.63	1.71	80
14	a	31	0	100	2	4.3	17.2	25	0.96		20*
15	a	15	0	100	3	4.5	27.0	100	0.48	3.42	50
16	c	15	1	100	0		0			1.23	100
17	c	15	1	100	2	8.0	16	100	0.40	1.41	100

All cases: (1) Tracers introduced over 10 transit times, (2) $R_Q=10^5$, and (3) $\hat{s} = (2\times10^{-8})Pe$.
* Used to test cases with n=15.

material are unobtainable. We can obtain the large-scale features of mixing, however, and these will give us insight into whether or not recycled material can be stored in specific layers or regions within the convecting system for long periods of time. These calculations should be considered exploratory in that their purpose is to map out the gross mixing and recycling phenomena expected when thermal and intrinsic density interact.

Results of Numerical Computations

The principal problem to be addressed is, Does the interaction of the large-scale flow and the intrinsic density of subducted material cause this material to accumulate in certain regions (for example at the bottom) and then prolong either the survival time of spatial heterogeneity or the length of tracer residence times? To address these questions, three forms of the calculations, each of increasing complexity, are presented: (1) cases with steady plate kinematics, (2) cases with unsteady plate kinematics and with tracers introduced over the first 10 transit times of the model run, and (3) cases with unsteady plate kinematics and with tracers introduced over the entire model run. The cases considered are summarized in Tables 2 and 3.

Steady Plate Kinematics

In the first cases considered, the plates are maintained in a steady configuration; although this has only marginal geological relevance, it illustrates basic mixing phenomena well. For simplicity the tracers are introduced only over the first 10 transit times of the model

TABLE 3. Summary of Mixing Computations With Intrinsic Density

Case	Plate Model	n	μ	A_Q	$N_{\bar{T}}$	$A_{\bar{T}}$	N_m	Γ_{peak}	Run Time
C1	s	15	1	2.0	9.5	19.0	100	0.68	60
C2	s	15	0	2.0	5.0	20.0	100	0.25	60
C3	a	15	1	0.5	8.3	4.2	50	0.36	70
C4	a	15	1	2.0	7.5	15.0	50	0.66	120*
C5	a	31	1	2.0	7.9	15.8	12	1.00	60
C6	a	31	1	6.0	7.1	42.6	12	0.58	60
C7	a	15	0	2.0	4.5	18.0	50	0.20	70
C8	a	15	0	6.0	3.5	42.0	25	0.48	60
C9	a	15	0	10.0	3.2	64.0	25	0.40	50

All cases: (1) Continuous introduction of tracers, (2) $R_Q=10^5$, (3) Pe=100, and (4) $\hat{s}=2\times10^{-6}$.
* Tracers sampled, all other cases tracers not sampled.

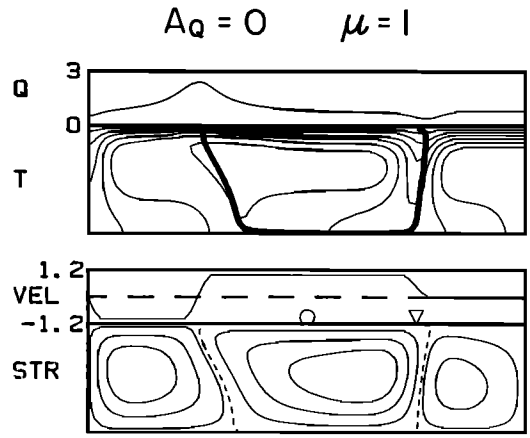

Fig. 3. Entry of passive tracers into a steady convective flow from a point source below the "trench" (triangle); this is case 1 in Table 2. The tracers are advected simply around the margin of the center cell, and all are sampled beneath the circle.

run. In Figure 3 the case with passive (A_Q=0) tracers after 10 transit times is shown. The principal features of Figure 3 are Q, the top surface heat flux, T, the isotherms and the positions of the tracers, and VEL, the imposed top surface velocity (positive to the right). The source and sink of the tracers are denoted by the triangle and circle, respectively. The ridge is the left center margin with symmetrical divergence, while the right center margin is the trench, with asymmetrical convergence. STR are the streamlines (the dashed one being the zero contour).

When the tracers are passive (A_Q = 0, Figure 3), they are simply advected by the flow. The tracers are placed beneath the trench and are on the edge of the center cell, where they remain; all are sampled near the ridge. When the tracers become negatively buoyant, however, they affect the flow as shown in Figure 4a (A_Q = 2). The tracers are again successively introduced at the edge of the center cell during the first 10 transit times, but when the tracers emerge from the bottom and start their ascent into the warm upwelling region, they slow and form a region of high spatial density; the heavy tracers neutralize the warm buoyant fluid. The streamlines are deflected from this neutralized region and indicate that the flow velocities are reduced considerably there. By time 20, in Figure 4b, the chemically anomalous region has settled into a quasi-steady structure; tracers are being swept back into the flow, but only at a small rate.

This behavior is dependent on the heating mode, which is varied from internal heating (μ=1, Figures 4a and 4b) to entirely bottom heating (μ =0, Figures 4c and 4d). With bottom heating, the tracers fail to disrupt the flow significantly, even when the density anomaly ratio A_Q remains constant. There is a moderate amount of clumping at the base of the rising

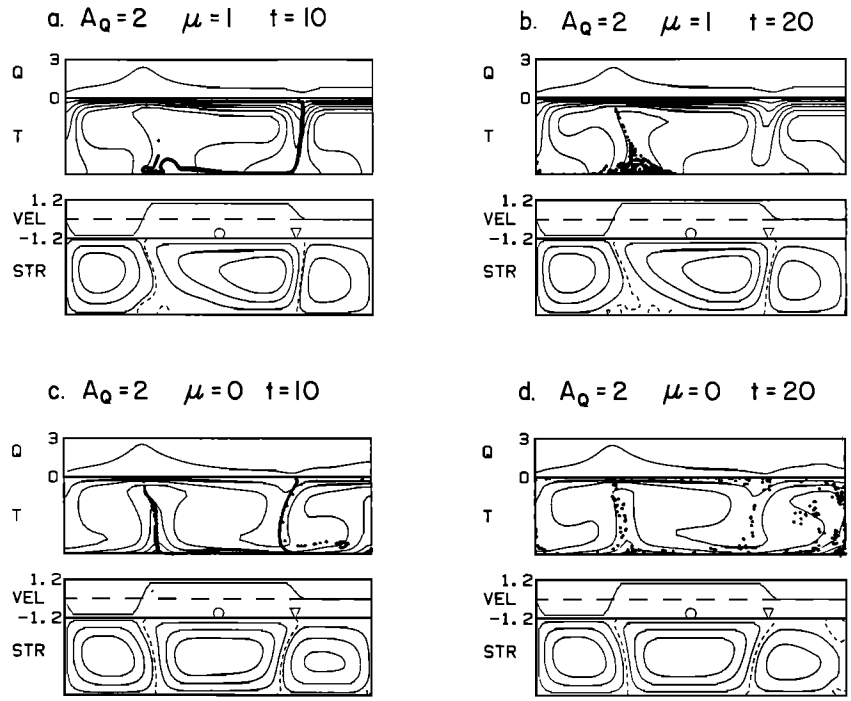

Fig. 4. Negatively buoyant tracers introduced into convective flows where the top boundary velocity has been held in a constant configuration. The density anomaly ratio (A_Q = 2) is constant for all cases. In internally heated flows (μ=1, in Figures 4a and 4b; case 2) the tracers segregate near the bottom of the warm upwelling region. However, in the bottom heated flows (μ=0, Figures 4c and 4d; case 3), the tracers can easily be swept by the flow and do not segregate to a significant extent. The times are in transit times.

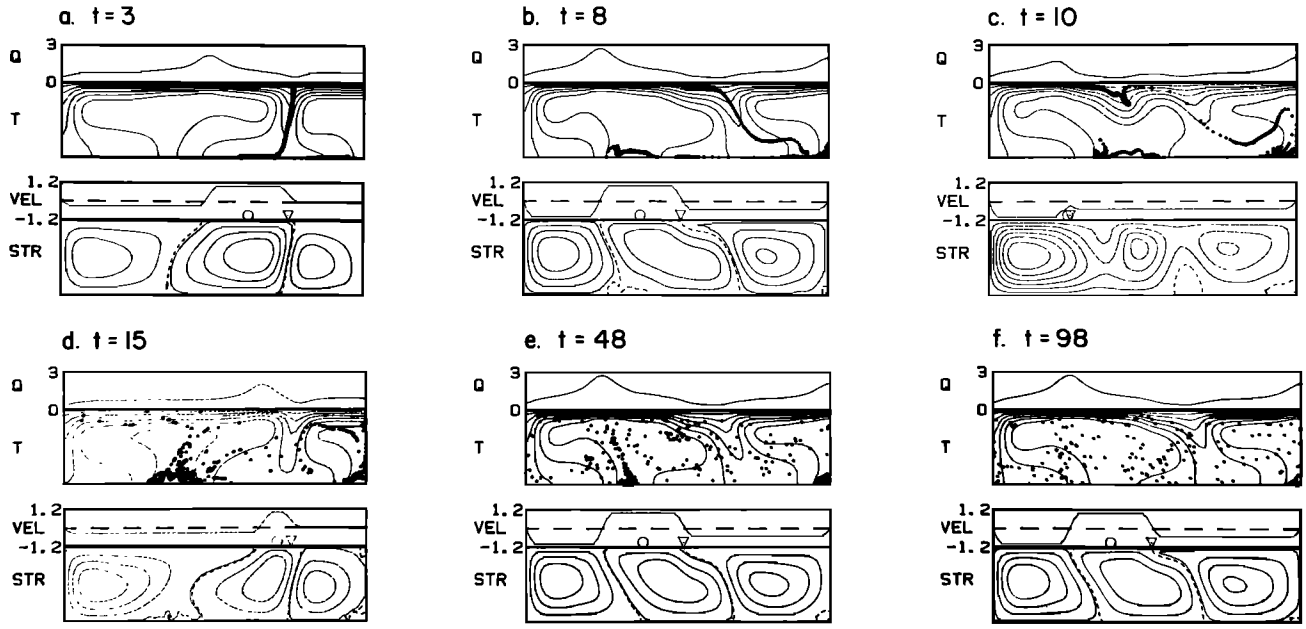

Fig. 5. Introduction of heavy tracers in an internally heated flow with unsteady velocity boundary conditions; in all cases, $R_Q = 10^5$ and $A_Q = 2$. The tracers were introduced during the first 10 transit times. The tracers segregate to the base of the warm upwelling regions, but these regions of neutralized buoyancy are eventually dissipated by the unsteady flow. The times are in transit times.

limb on the right, but the tracer clumping is of less significance than in the internally heated case. The tracers cannot easily neutralize the strongly buoyant (hot) thermal boundary layer along the bottom and remain closely positioned around the margins of the cells. The tracers are easily swept along by "thermal" convection.

Unsteady Plate Kinematics

As discussed at length in paper 1, plate rearrangements and migration of plate margins are fundamental features of plate kinematics. Plate kinematics can be categorized into general rules (for example, symmetrical spreading at ridges), which can be simply introduced into the numerical calculations. Unfortunately, the long-term unsteady behavior of plate motion is uncertain, so as a first approximation the plate rearrangement is assumed to be periodic in time; the effect of this approximation will be tested at the end of this section.

In order to elucidate the effects of unsteady large-scale flow, case 6, with $A_Q = 2$, will be considered in detail. The plate model a, in Table 2, for this case has been discussed in detail in paper 1; briefly, however, a ridge is initially located at x=1 and a trench at x=3; the ridge migrates toward the trench, and the two margins coalesce at time 6; a new trench forms at the point of collision and migrates to the left, until the trench coalesces with a new ridge at x=1; the sequence repeats. In Figure 5 the first frame (time 3) is before the ridge and trench coalesce. Because the trench remains approximately stationary with respect to the margin of the cells, the tracers are consecutively positioned around the margin of the center cell up to about t=5. Frame b at time 8 shows tracers being placed below the "trench" as it migrates toward the left. Near the bottom of the warm upwelling region the tracers form a high-density patch, similar to the one that formed with the steady plates (Figure 4a); this region tends to persist to about 50 transit times. A similar phenomenon occurs under the upwelling region on the right, and the clumped tracers tend to persist there for more than 100 transit times (frame f of Figure 5 is at t=98). The position of the clumps of tracers is due to the neutralization of the thermal buoyancy by the negatively buoyant tracers. Only a small fraction of the tracers is actually resting on the bottom, and many are actually "floating" a small distance from the bottom. However, the continued rearrangement of the surface plates, which causes the large-scale convection cells to grow and shrink, tends to continuously erode tracers off the sides of the chemically anomalous regions. The neutrally buoyant regions dissipate. The right anomaly persists longer than the central anomaly and is due to the spatial persistence of the warm upwelling region on the right.

The effect of the heating mode is explored with case 13, where the flow is driven by heat entering through the bottom, but $A_Q = 2$ as is case 6, just described. The most striking difference between case 6 and this one is the lack of large diffuse regions of tracers near the bottom. Tracers did tend to preferentially clump near the base of the uprising limbs, as in the steady case. This case confirms the results from the steady plate cases described above: neutralization of buoyancy occurs at a higher A_Q for bottom heating as opposed to internal heating when the total heat remains constant.

The use of periodic plate models is potentially

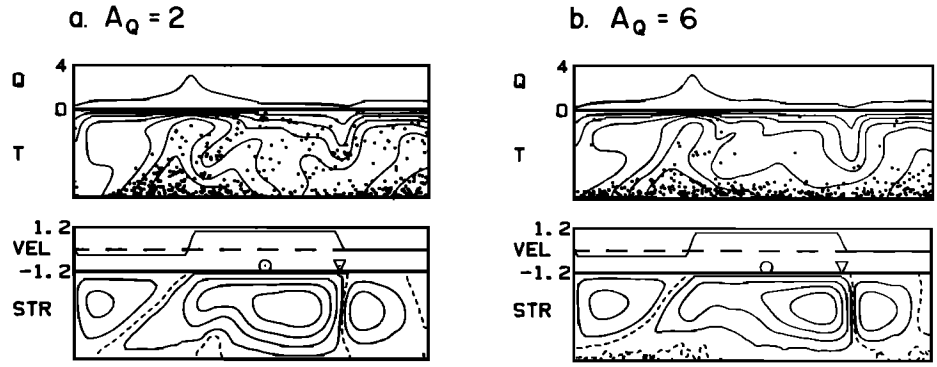

Fig. 6. Continuous introduction of heavy tracers into an internally heated flow after 61 transit times for (a) $A_Q = 2$ and (b) $A_Q = 6$. The transition to clear layering is rather indistinct but probably occurs somewhat above 6.

a significant approximation. When the tracers are passive, periodic plate evolution produced no spurious effects on mixing (paper 1). To test the effect of the periodic plate model, the same pseudorandom model from paper 1 has been employed. Plate model c of Table 2 (discussed in paper 1) has 26 stages of plate evolution arranged in a pseudorandom fashion. Qualitatively, the fluid phenomena displayed by case 17 are essentially the same as in case 6 (Figure 5), but now the warm regions of upwelling are more mobile (because of the greater degree of plate rearrangement), and the diffuse regions of heavy tracers tend to waft back and forth across the bottom.

Continuous Introduction of Tracers

In the final set of calculations, the tracers are introduced throughout the model run instead of the first 10 transit times. This was done to explore the interaction between newly introduced tracers and "older" tracers, on the one hand, and to approximately determine the value of A_Q for which layering sets in, on the other.

The tracers are introduced throughout the model run when the plates are steady (cases C1 and C2, Table 3). For the internally heated case (C1) there is no change from case 2 when the tracers were introduced over the first 10 transit times. But for the bottom heated case (C2), tracers accumulate and neutralize the buoyancy near the bottom of the hot limbs. However, the neutralized regions apparently become hotter more rapidly than tracers are added, and the stagnant regions eventually become thermally unstable and break up. This time-dependent phenomenon did not occur when $\mu = 1$. Furthermore, this behavior is unique to the steady state plate cases and did not occur when there was plate rearrangement (case C7).

In Figure 6, two cases with internal heating after 61 transit times are shown; case C5 has $A_Q = 2$ and C6 has $A_Q = 6$. The transition from regions of neutralized buoyancy beneath warm upwelling regions to clearly defined chemical layering is rather indistinct. In the case of $A_Q = 2$ there is a higher proportion of tracers through the bottom 1/4 of the box, but the distribution is not smooth, as there is a lack of tracers at the base of the downwelling regions. Increasing A_Q to 6, the bottom half starts to develop convection cells distinct from the cells defining the top surface motions. There is a distinct lack of tracers in the top two-thirds, but there is still no sharp boundary between convecting layers as defined by the tracers. True two-layer convection will not form until even higher A_Q.

Residence Times

The residence time t_r is defined as the average time tracers remain in the box from subduction to sampling beneath the ridge. The residence time provides an economical characterization of the average age of the convecting system and is potentially related to the observed apparent isochrons of midocean ridge basalts (MORB), defined on a global scale [Chase, 1981; Davies, 1984].

For passive tracers, Gurnis and Davies [1986] have shown that (1) tracer sampling is well approximated by a random sampling model and (2) the true residence time t_r is well approximated by the flux time t_f; t_f is the time it takes for an area equivalent to the box area to flux through a sampling region of depth d_s:

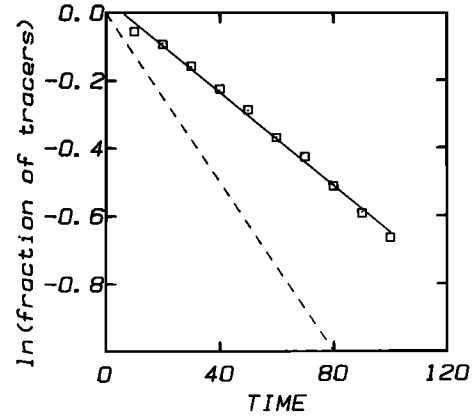

Fig. 7. Fraction of tracers in the box for case 6 (squares), which is shown in Figure 5. The dashed line is expected for passive tracers; the solid line is a linear regression of the data values. The time constant for the rate of sampling has increased by a factor of 1.8 when A_Q is increased from 0 to 2.

TABLE 4. Summary of Model Results and Comparison With Mantle Values

Mantle Parameter	Model Parameter	Upper Mantle Convection		Whole-Mantle Convection	
		Complete Separation of Oceanic Crust	Lithosphere Remains Layered	Complete Separation of Oceanic Crust	Lithosphere Remains Layered
$\Delta\rho$ (kg/m^3)		200	10	200	10
R_C		6.8×10^5	3.4×10^4	5.4×10^7	2.7×10^6
R_T		3.3×10^5	3.3×10^5	3.0×10^7	3.0×10^7
R_Q		4.5×10^6	4.5×10^6	1.7×10^9	1.7×10^9
A_Q		0.15	0.008	0.03	0.0016
	Minimum A_Q neutralization of buoyancy	(0.19)	(0.038)	(0.04)	(0.008)
	Minimum A_Q chemical layering	(0.97)	(0.19)	(0.53)	(0.1)
A_T		2.1	0.11	1.8	0.09
	Minimum A_T neutralization of buoyancy	(4.5)	(0.9)	(4.2)	(0.84)
	Minimum A_T chemical layering	(16)	(3.2)	(43)	(8.6)
	Maximum increase in residence time, %	15	4	13	3

Model values are in parentheses.

$$t_f = \frac{S}{d_s u_b} = \frac{S\,Ra}{d_s\,Pe} \qquad (10)$$

where S is the area of the box and u_b is the average boundary velocity (see Appendix A). In (10) all quantities are nondimensional. Gurnis and Davies have shown that if the tracers are randomly sampled, then the number of tracers remaining in the box as a function of time decays exponentially with a decay constant of t_f:

$$N(t) = N_o e^{-t/t_f} \qquad (11)$$

In Figure 7, the fraction of tracers remaining in the box (N/N_o) as a function of transit time is shown for case 6, which has an A_Q of 2 (see also Figure 5). The dashed curve is for t_f = 80 (see Figure 9 of paper 1), and the solid line is a regression through the values from case 6 with a time constant τ. The τ/t_f, and consequently, the residence time t_r has been increased by a factor of 1.8 when A_Q was increased from zero to 2. Moreover, there was a further increase in τ/t_f (case C4) of 5-10% when the tracers were introduced for the entire model run.

Scaling to the Mantle and Conclusions

The interaction of intrinsic buoyancy and large-scale thermal convection has been explored. The source of the intrinsic buoyancy is the subduction of chemically distinct oceanic lithosphere. The results are summarized in Table 4 for both upper mantle and whole-mantle convection. In Table 4, values resulting from the modeling are in parentheses all other quantities are estimated mantle values for the different scenarios listed. Moreover, two rather extreme scenarios

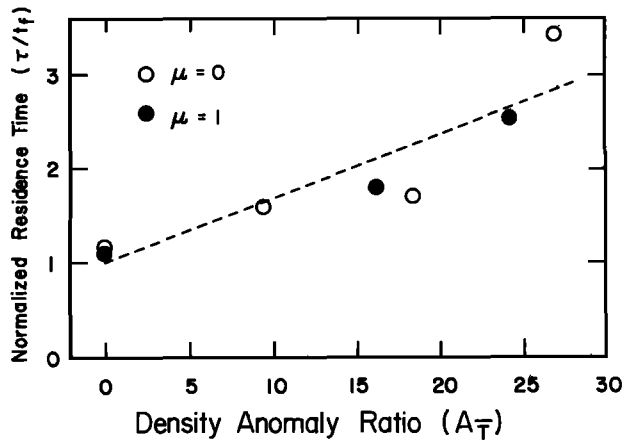

Fig. 8. Increase of the sampling time constant τ/t_f (and hence residence time) as a function of density anomaly ratio A_T, for two heating modes (μ=0, bottom heating; μ=1, internal heating). The dashed line is a linear regression (see (8)).

of the subduction of anomalous material have been considered. In the first case, oceanic crust is assumed to efficiently separate from the rest of the lithosphere and to have a $\Delta\rho$ = 200 kg m^{-3} [Anderson, 1979; Ringwood, 1975, 1982]. In the second case, the lithosphere remains layered after subduction, and an upper limit is placed on its integrated density difference. This integrated density is judged to be 10 kg m^{-3}, at the very most (from the data summarized by Ringwood [1982]) and may well be only 1/10 to 1/100 of this value.

The procedure for scaling density anomalies is presented in Appendix C. Since A_Q depends on R_Q while A_T does not, scaled results are discussed in terms of A_T. However, the scalings were made using both definitions and are summarized in Table 4. The density anomaly ratios at which certain mixing behavior set in (summarized in Table 4) are judged to be accurate to within about a factor of 2. This uncertainty arises not only from the rather qualitative judgment at which the stated mixing phenomena sets in but also from an uncertainty in the mantle Rayleigh and Nusselt numbers. This uncertainty is reflected in the factor of 2 difference between the mantle value/model value for the A_T values compared with the A_Q values in Table 4.

In bottom-heated convection scaled to the upper mantle, crust subducting alone can rest near the base of the upwelling limbs of convection cells if $A_T > 4.5$ and will start to form a layer of chemically anomalous material if $A_T > 16$. For upper mantle parameters, $A_T < 2.1$, which suggests some neutralization could take place if crust separated efficiently from the rest of the lithosphere. By rescaling the flux to the entire lithosphere (see Appendix B), instead of to just the crust, we find that neutralization of thermal buoyancy sets in at A_T = 0.9 and layering sets in at > 3.2 if crust remains layered with the lithosphere; an upper limit on the A_T for this mantle scenario is only 0.11, which is sufficiently small to preclude neutralization of thermal buoyancy.

In internally heated convection scaled to the whole mantle, crust subducting separately can form diffuse regions of neutralized buoyancy through the base of warm upwelling regions if $A_T > 4.2$ and can start to form a layer at the base if $A_T > 43$. For parameters appropriate to whole-mantle convection, A_T is 1.8, and thus neutralization is again marginally possible. The values for the complete lithosphere are $A_T > 0.84$ (for localized neutralization) and $A_T > 9$ (for layering); the mantle A_T is less than 0.09; thus it seems unlikely intrinsic density could play much of a role in the whole-mantle convection scenario, unless crust efficiently separates from the underlying lithosphere.

The dependence of the residence time on the intrinsic density is presented in Figure 8. When the tracers have excess negative buoyancy, sampling becomes sluggish and τ/t_f increases from unity. In the figure, only those cases with periodic plate evolution, with $R_Q = 10^5$ and $Pe = 10^2$, and with tracers introduced over 10 transit times have been plotted; the heating mode and density anomaly ratio vary. The open circles are for bottom heating (μ=0), and the solid circles for internal heating (μ=1). The residence times appear to be independent of heating mode. The dashed line in Figure 8 has the form

$$(\tau/t_f) = 1.0 + (0.07)\, A_T \qquad (12)$$

Using this relation, scalings are made for the different geological scenarios of Table 4. Thus with the upper limits to mantle A_T's, τ/t_f could be increased by as much as 14% for crust subducting separately into the mantle and by 4% for the case where crust and lithosphere remain layered.

The residence time can be used to calculate model mean ages for the mantle, as was shown in paper 1. The model mean age of the mantle, resulting from the recycling of passive material, is between 600 m.y. and 1.3 b.y. for upper mantle convection and 900 m.y. and 2.5 b.y. for whole-mantle convection. These model ages result from a consideration of a wide range of model parameters, including increased rates of convection in the past. For whole-mantle convection, these ages are consistent with the apparent Pb-Pb and Rb-Sr isochrons for MORB and oceanic island basalts (OIB) [cf. Brooks et al., 1976; Chase, 1981], the addition of intrinsic density does not significantly alter this result, even for the fairly extreme scenario of oceanic crust that separates entirely from the rest of the lithosphere.

It is unlikely that the intrinsic density of subducting oceanic lithosphere can have much effect on mantle dynamics and therefore on the chemical evolution of the mantle. Assuming the oceanic crust can separate from the rest of the lithosphere, it is marginally possible for the crust to neutralize the thermal buoyancy near the bases of hot upwelling regions, but even in this extreme scenario, the residence time could not be increased by more than 14%.

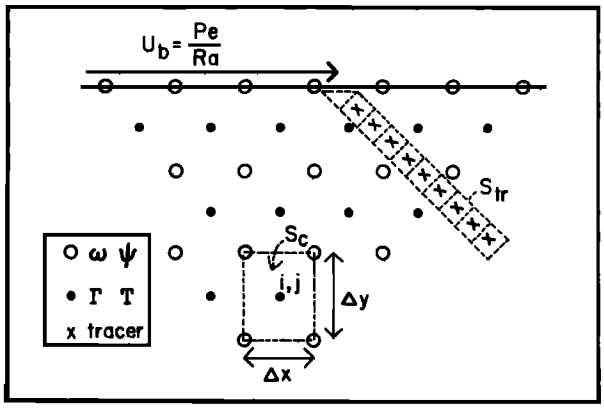

Fig. 9. Schematic of numerical grid showing the staggered grid for the T (and Γ) and ψ (and ω) fields. S_{tr} is an implicit area assigned to the tracers, and Δt is the time between introduction of individual tracers. S_c is an area surrounding the Γ grids. The value of Γ at ij is proportional to the number of tracers falling within S_c. Other quantities are defined in the text.

Models or hypotheses that assume that intrinsic density plays a pivotal role will have to be reconsidered in light of these calculations.

Appendix A: Mathematical Formulation

The equations of motion are solved in a two-dimensional rectangular region with an aspect ratio (width to depth) of 4:1 and with uniform Newtonian viscosity. The buoyancy forces arise from both thermal expansion and spatial variations in intrinsic density; other variations in density are assumed to be negligible, and the Boussinesq approximation is employed. The form of the anomalous density variation is

$$\rho = -\rho_o \alpha (T - T_o) + \Delta\rho \qquad (A1)$$

and $\rho << \rho_o$. Here Δρ is the density difference between a parcel of fluid of ambient density ρ_o and a parcel of fluid with intrinsic chemical density.

When lengths are normalized by D, the box depth, the temperatures by ΔT, a temperature scale defined below, and the velocities by

$$V_o = \frac{g \alpha D^2 \Delta T}{\nu} \qquad (A2)$$

where ν is the kinematic viscosity, the heat and momentum equations are, respectively

$$\frac{\partial T}{\partial t} + \frac{\partial}{\partial x}(v_x T) + \frac{\partial}{\partial y}(v_y T) = \frac{1}{Ra}(\nabla^2 T + \mu) \qquad (A3)$$

and

$$\nabla^4 \psi = \frac{\partial T}{\partial x} - \frac{Rc}{Ra}\frac{\partial \Gamma}{\partial x} = \frac{\partial T}{\partial x} - A\frac{\partial \Gamma}{\partial x} \qquad (A4)$$

All quantities in (A3) and (A4) are nondimensional; t is time, x and y are the horizontal (positive to the right) and vertical (positive upward) distances, v_x and v_y are the horizontal and vertical velocity, ψ is the stream function defined below, Γ is the fraction of anomalous material in an infinitesimal area (and is comparable to f_m in (1)), A is the density anomaly ratio, and μ is defined as

$$\mu = \frac{H D^2}{K \Delta T} \qquad (A5)$$

where H is the rate of internal heat generation per unit volume. The total heat flux Q is

$$Q = Q_b + HD \qquad (A6)$$

where Q_b is the heat flux at the bottom boundary. The stream function is defined through

$$v_x = \frac{\partial \psi}{\partial y} \qquad v_y = -\frac{\partial \psi}{\partial x} \qquad (A8)$$

On the top surface of the box, the velocity is imposed; a Peclet number is defined as

$$Pe = \frac{D U_b}{\kappa} \qquad (A9)$$

where U_b is the top boundary velocity. Furthermore, a nondimensional boundary velocity is defined as $u_b = U_b/V_o = Pe/Ra$.

Appendix B: Numerical Procedure

The heat and momentum equations (A3) and (A4) are solved on a discrete mesh with finite differences. The solution of the heat equation is unaffected by the addition of intrinsic density, and the alternating direction implicit (ADI) method is used [Lux, 1978]. The actual solution of the momentum equation remains unchanged from paper 1 (an efficient cyclic reduction method is used [Sweet, 1974]), but now the right-hand side of the biharmonic equation (A4) is a function of both the temperature field and the tracer positions. In addition to the normal ψ and T grids, there is also a mesh of the fraction of anomalous material within a mesh Γ. At any time the coordinates (x and y) of the tracers are known and the positions are integrated forward using a predictor corrector method (see paper 1). The Γ array is then recalculated after tracer advection, so that the fraction of anomalous material within a cell of size Δx Δy around a mesh point is found. Γ at mesh i,j is

$$\Gamma_{ij} = \frac{N_{ij}}{N_m} \qquad (B1)$$

where N_{ij} is the number of tracers in cell ij and N_m is the "maximum" number of tracers that could fit in a cell, assuming each tracer had a certain volume. From Figure 9, N_m is

$$N_m = \frac{S_c}{S_{tr}} = \frac{S_c}{\dot{s}\,\Delta t} = \frac{\Delta x\,\Delta y}{\delta w\, u_b\, \Delta t} \qquad (B2)$$

where S_c is the area of one cell, S_{tr} is the

"equivalent" area of a single tracer, $\hat{s}$ is the nondimensional flux defined in (9), δw is the normalized thickness of anomalous material, u_b is defined in Appendix A, and Δt is the time between tracer introductions. If δw is increased by a factor of 5 (=30km/6 km) when scaling the flux from crust to lithosphere and the value of A is decreased to 1/5 of its value, then the value of A $\partial\Gamma/\partial x$ in (A4) remains unchanged.

The use of an implicit thickness of the anomalous material δw, smaller than the mesh spacing, does not introduce spurious mixing. First, it was shown in the main text that unless subducted crust is concentrated through a fairly large volume (hundreds of kilometers) then the Stokes velocity is much smaller than the plate velocity. For comparable parameters, this means that a single "tracer" has a negligible velocity. Second, the Stokes velocity in the two-dimensional models is independent of the radius, for a constant anomalous mass. It can be shown [cf. Batchelor, 1967] that the two-dimensional Stokes velocity has the form

$$U_c \propto \frac{g\,\delta\sigma\,a^2}{\eta} \qquad (B3)$$

where $\delta\sigma$ is the two-dimensional density. If the two-dimensional mass is $\delta\theta$ (= $\delta\sigma\ \pi\ a^2$), where a is the radius of the area that the mass is averaged over), then the Stokes velocity is

$$U_c \propto \frac{g\,\delta\theta}{\eta} \qquad (B4)$$

If $\delta\theta$ is the mass of a tracer (or a clump of them), then the two-dimensional Stokes velocity is independent of the mesh spacing they are averaged over. Therefore the rather coarse mesh used here should not introduce spurious effects. This was confirmed when some of the cases originally computed using a 16x64 mesh were recomputed using a 32x128 mesh.

Appendix C: Scaling the Transition Density Anomaly Ratios

The transition value of A_Q, used for the computations, depends on the Rayleigh number, as shown below. The transition values will be denoted in this section as A'_Q and A'_T. To scale the model results to the mantle, either an A'_Q appropriate to mantle R_Q's can be found, or alternatively, an A_T, which is independent of R_Q, can be found. In this section the definitions and notation of Davies [1986] are followed where appropriate.

First, the relation is found between A'_Q and A'_T. The density anomaly ratio, in terms of a constant heat flux has been defined as (8)

$$A_Q = \frac{K\,\Delta\rho}{\rho_o\,\alpha\,D\,Q} \qquad (C1)$$

The Nusselt number is defined in general as

$$Nu = Q/q_c \qquad (C2)$$

where q_c is the heat that would be conducted in the absence of convection. When the heat flux is held constant, the average temperature can be found across the bottom, $\bar{T}_b$, and therefore an approximate conductive heat flux can be defined as

$$\bar{q}_c = K(\bar{T}_b - T_t)/D \qquad (C3)$$

A Nusselt number can then be defined as

$$N_{\bar{T}} = Q/\bar{q}_c \qquad (C4)$$

Substituting (C4) into (C1),

$$A'_Q = \frac{\Delta\rho}{\rho_o\alpha\,(\bar{T}_b - T_t)}\,N_{\bar{T}}^{-1} = A'_{\bar{T}}/N_{\bar{T}} \qquad (C5)$$

So

$$A'_{\bar{T}} = N_{\bar{T}}\,A'_Q \qquad (C6)$$

which is approximately equal to A'_T, defined in (7), and therefore independent of the Rayleigh number. For a model run with an A'_Q already known, an $A'_{\bar{T}}$ can be found that can be compared with mantle A'_T's.

An alternative method of scaling is to find the A'_Q appropriate to the mantle R_Q. The dependence of A'_Q on R_Q can be found by considering the Nusselt-Rayleigh number relation [cf. Davies, 1986]

$$Nu = \frac{Q}{q_c} = c\,R_Q^{1/4} \qquad (C7)$$

where c is a constant and R_Q is the Rayleigh number defined in (5). Substituting (C7) into (C1), and using the scale $q_c = K\,\Delta T/D$, we find

$$A'_Q = \frac{A'_T}{c}\,R_Q^{-1/4} = c'\,R_Q^{-1/4} \qquad (C8)$$

which can be used to find A'_Q's appropriate for mantle R_Q's.

In order to most closely match mantle and model parameters, the actual mantle temperature difference $(T_b - T_t)$ in A_T (defined in (7)) is taken to be the temperature difference across the lithosphere (the top thermal boundary layer). This quantity can be evaluated for the mantle from the cooling of the oceanic lithosphere [Parsons and Sclater, 1977; Cazenave, 1984]. In (C3), $(\bar{T}_b - T_t)$ is then approximately the temperature difference across the top boundary layer for internally heated convection and $(\bar{T}_b - T_t)/2$ for bottom heated convection. Therefore for the bottom heated (μ=0) cases, the scaling

$$A'_{\bar{T}} = 2N_{\bar{T}}\,A'_Q \qquad (C9)$$

is used in lieu of (C6).

Acknowledgments. I wish to thank G. Davies and R. Griffiths for advice on these calculations, and G. Davies, G. Houseman, P. Olson, A. E. Ringwood, and D. J. Stevenson for comments on this manuscript.

References

Anderson, D. L., The upper mantle transition region: ecologite?, Geophys. Res. Lett., 6, 433-435, 1979.

Anderson, D. L., Isotopic evolution of the mantle, Earth Planet. Sci. Lett., 57, 13-24, 1982.

Batchelor, G. K., An Introduction to Fluid Mechanics, 615 pp., Cambridge University Press, New York, 1967.

Brooks, C., S. R. Hart, A. W. Hofmann, and D. E. James., Rb-Sr mantle isochrones from oceanic regions, Earth Planet. Sci. Lett., 32, 51-61, 1976.

Cathles, L. M., The Viscosity of the Earth's Mantle, Princeton University Press, Princeton, N.J., 1975.

Cazenave, A., Thermal cooling of the oceanic lithosphere: New constraints from geoid height data, Earth Planet. Sci. Lett., 70, 395-406, 1984.

Chase, C. G., The n-plate problem of plate tectonics, Geophys. J. R. astr. Soc., 29, 117-122, 1972.

Chase, C. G., Oceanic island lead: Two-stage histories and mantle evolution, Earth Planet. Sci. Lett., 52, 277-284, 1981.

Davies, G. F., Review of oceanic and global heat flow estimates, Rev. Geophys. Space Phys., 18, 718-722, 1980.

Davies, G. F., Geophysical and isotopic constraints on mantle convection: An interim synthesis, J. Geophys. Res., 89, 6017-6040, 1984.

Davies, G. F., Mantle convection under simulated plates: effects of heating modes and ridge and trench migration, and implications for the core-mantle boundary, bathymetry, the geiod, and Benioff zones, Geophys. J. R. astr. Soc., 84, 153-183, 1986.

Gurnis, M. and G. F. Davies, Mixing in numerical models of mantle convection incorporating plate kinematics, J. Geophys. Res., 91, 6375-6395, 1986.

Hager, B. H., Subducted slabs and the geoid: Constraints on mantle rheology and flow, J. Geophys. Res., 89, 6003-6015, 1984.

Hofmann, A. W. and W. M. White, Mantle plumes from ancient oceanic crust, Earth Planet. Sci. Lett., 57, 421-436, 1982.

Lux, R. A., The effects of a moving lithospheric plate on convection in the earth's mantle, Ph.D. thesis, 87 pp., Univ. of Rochester, New York, 1978.

McKenzie, D. P., J. M. Roberts, and N. O. Weiss, Convection in the earth's mantle: Towards a numerical simulation, J. Fluid Mech., 62, 465-538, 1974.

O'Connell, R. J. and B. H. Hager, Velocity anomalies, convection, heat transport and viscosity of the lower mantle (abstract), EOS Trans. AGU, 65, 1093, 1984.

Parsons, B., and J. G. Sclater, An analysis of the variation of ocean floor bathymetry and heat flow with age, J. Geophys. Res., 82, 803-827, 1977.

Peltier, W. R., Ice Age geodynamics, Ann. Rev. Earth Planet. Sci., 9, 199-225, 1981.

Richter, F. M., On the driving mechanism of plate tectonics, Tectonophsics, 38, 61-68, 1977.

Ringwood, A. E., Composition and Petrology of the Earth's Mantle, 618 pp., McGraw-Hill, New York, 1975.

Ringwood, A. E., Phase transformations and differentiation in subducted lithosphere: Implications for mantle dynamics, basalt petrogenesis, and crustal evolution, J. Geol., 90, 611-643, 1982.

Sweet, R. A., A generalized cyclic reduction algorithm, SIAM J. Numer. Anal., 11, 506-520, 1974.

Turcotte, D. L. and G. Schubert, Geodynamics, 450 pp., John Wiley, New York, 1982.

Yuen, D. A., W. R. Peltier, and G. Schubert, On the existence of a second scale of convection in the upper mantle, Geophys. J. R. astr. Soc., 65, 171-190, 1981.

Yuen, D. A., R. Sabadini, E. V. Boschi, Viscosity of the lower mantle as inferred from rotational data, J. Geophys. Res., 87, 10745-10762, 1982.

M. Gurnis, Research School of Earth Sciences, Australian National University, GPO Box 4, Canberra, ACT 2601, Australia.

(Received November 27, 1985;
revised May 9, 1986;
accepted May 30, 1986.)